BIOCHIP JOURNAL, Vol. 1, No. 4, 281-287, December 2007

Plasmonic Biosensor

Hyeon-Bong Pyo[1], **Moon Youn Jung**[1] **&**
Seon-Hee Park[1]

[1]IT Convergence and Components Laboratory, Electronics and Telecommunications Research Institute, Daejeon 305-700, Korea
Correspondence and requests for materials should be addressed to H.-B. Pyo (pyo@etri.re.kr)

Accepted 5 November 2007

Abstract

Issues on optical and physical characteristics of plasmonic biosensor were described. Starting from physical principles of surface plasmons, resonant coupling, and dispersion, we then discussed more practical and essentially important aspects on dielectric functions, penetration depth, and functional differences in SPR imaging systems. Scaling procedure from experimentally obtained SPR curve to incident angle was also discussed. Also, physical background of plasmon-resonant, extinction-, scattering- and near-field cross-section of metallic nanoparticles was briefly explained, based on Mie scattering. Extinction spectra were calculated for various sizes of gold and silver nanoparticles and compared with experimentally observed extinction spectra for colloidal gold.

Keywords: Plasmonic biosensor, Surface plasmon resonance (SPR), Dispersion relation, Evanescent field, Total internal reflection (TIR), SPR imaging, Localized surface plasmon resonance (LSPR), Extinction spectra

Introduction

Surface plasmon polaritons or simply surface plasmons (SPs) are a longitudinal, collective, and coherent oscillation mode of electrons on the metal surface. They are confined within a Fermi wavelength scale ($\sim$O (Å)), whereas they propagate along the metal-dielectric interface until they lose their energies into Joule heat. Propagation length depends on the optical properties of metal and dielectric adjacent to the metal layer[1,2]. Parameters which determine the characteristics of plasmons are (1) dielectric function of materials, of which the system is consisted, (2) geometric configuration, the thickness of layers, (3) energy or wavelength, at which we are monitoring the system, and (4) angle of incident light. Further, if we consider an ensemble of metallic nanoparticles in a dielectric medium, the shape and size of the particles would be important parameters for optical manipulation. In all, dispersion relation of SPs determines the whole dynamics of the system.

Surface plasmon resonance (SPR) is an energy transfer from an external source to the SPs. Traditionally, electron energy loss spectroscopy (EELS) has been used to investigate a system of SPs, which cannot be coupled with visible light in normal condition. However, after the invention of Kretschmann and Raether[1], a total internal reflection (TIR)-based coupling method has become a very popular tool to explore an SP system in the visible region.

Starting from Maxwell equations with continuity conditions of the fields, we observe that dispersion relation of SPs is given as (see Figure 1)

$$k_{sp}=\frac{\omega}{c}\sqrt{\frac{\varepsilon_1(\omega)\varepsilon_2}{\varepsilon_1(\omega)+\varepsilon_2}}=\frac{2\pi}{\lambda}\sqrt{\frac{\varepsilon_1(\lambda)\varepsilon_2}{\varepsilon_1(\lambda)+\varepsilon_2}} \qquad \text{(eq. 1.1)}$$

which is completely determined by SP wavevector k_{sp} and (complex) dielectric functions of metal $\varepsilon_1(\omega)$ and dielectric ε_2, respectively, at a given wavelength. When light is illuminated on a plasmon-supporting metal layer with an incident angle θ_0, the amount of wavevector that can be coupled with surface plasmon mode is

$$k_x=\frac{\omega}{c}\sin\theta_0=\frac{2\pi}{\lambda}\sin\theta_0 \qquad \text{(eq. 1.2)}$$

because only x-component of wavevector can be coupled to the SPs which is an intrinsic longitudinal mode (TM-mode) of oscillation. From dispersion relations eqs (1.1) and (1.2) we conclude that the momentum of light in vacuum is always smaller than that of SPs so it cannot be resonantly coupled. To circumvent this problem, we can add an additional highly refractive (refractive index $\sqrt{\varepsilon_0}=n_0$) dielectric material in front of metal layer to couple the light to the SPs. This TIR coupling enables the enhancement of light wavevector so that the incident light can be coupled to SPs,

$$k_x=\frac{\omega}{c}\sqrt{\varepsilon_0}\sin\theta_0=\frac{\omega}{c}n_0\sin\theta_0=k_{sp} \qquad \text{(eq. 1.3)}$$

which is equivalent to

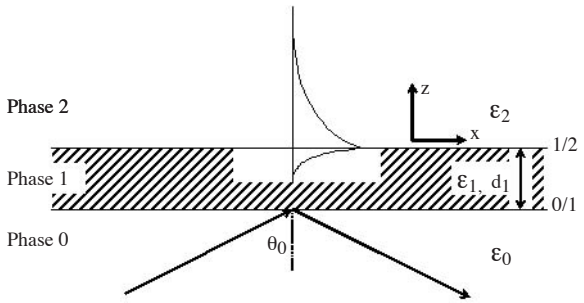

Figure 1. Three phases of SPR sensor configuration model to calculate reflectivity as a function of incident angle or wavelength. Phase 0, phase 1 and phase 2 are prism, metal layer, and dielectric, respectively.

$$n_0 \sin\theta_0 = \sqrt{\frac{\varepsilon_1(\omega)\varepsilon_2}{\varepsilon_1(\omega)+\varepsilon_2}} = \frac{2\pi}{\lambda}\sqrt{\frac{\varepsilon_1(\lambda)\varepsilon_2}{\varepsilon_1(\lambda)+\varepsilon_2}}. \quad \text{(eq. 1.4)}$$

Eq. (1.4) manifests itself an important tuning mode of SPR-based sensor: Let us consider if the refractive index and/or the thickness of dielectric material has changed for some reason. Then the dielectric function ε_2 will be changed, so to retain the SPR condition eq. (1.4), we can change either incident angle θ_0 at a fixed wavelength, or the wavelength λ at a fixed angle. These two modes are the main interrogation methods which have been used in biosensors. An alternative to them is an intensity difference-based imaging; although not at one point but over the whole sensor surface. This is usually known as surface plasmon resonance imaging (SPR imaging) or in older term, surface plasmon microscopy (SPM).

In this paper, we will consider a set of issues which we think of practical importance in using a SPR-based biosensor and system. Especially, issues on signal transduction, evanescent nature of plasmon field, dispersion, linearity, configuration of two- and zero-dimensional SPR sensor, and their specific characteristics will be discussed.

Dispersion Data

Dielectric function $\varepsilon(\lambda)$, dispersion data, or nk-values of materials is a function of energy. More important, yet not well recognized, fact is that it also depends on pressure, temperature, ambient, and phase (bulk or film) of material. Whether it was obtained in vacuum or in aqueous ambient, one must be cautious in the values of data whether it is appropriate to experimental situation to be applied. Figure 2 is a representative discrepancy in dispersion data for gold.

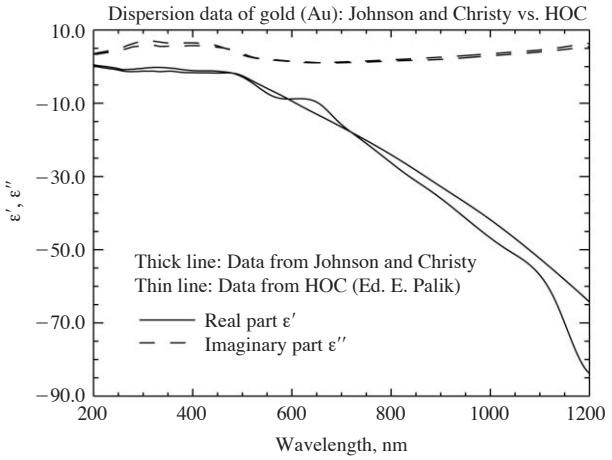

Figure 2. Comparison of two dispersion data for gold: Data from Johnson and Christy[3] and from Handbook of Optical Constants of Solids[4]. Especially, discrepancy of functional values in real part of dielectric function is dominant in visible and near-infrared region.

Refractive index $n(\lambda)$ and extinction coefficient $k(\lambda)$ are related to dielectric function as

$$\varepsilon(\lambda)=\varepsilon'(\lambda)+i\varepsilon''(\lambda)=(n(\lambda)+ik(\lambda))^2 = (n(\lambda)^2-k(\lambda)^2)+i2n(\lambda)k(\lambda) \quad \text{(eq. 2.1)}$$

Surface plasmon resonance occurs only when the real part of dielectric function $\varepsilon'_1(\lambda)<0$, whereas that of dielectric satisfies the condition $\varepsilon'_2(\lambda)>0$.

Penetration Depth of the Field

Surface plasmon field is a surface bound, non-radiative, and an evanescent field. It decays exponentially away from metal-dielectric interface normal to both sides. To estimate the sensitivity of a SPR sensor, a good measure of it would be the penetration depth, at which field intensity decreases in 36.8% ($\sim e^{-|\kappa|z}=e^{-1}$) of maximum field. For example, if we consider a 3-phase system as shown in Figure 1 as one of the simplest sensor configuration, we can immediately calculate the penetration depth of the field for metal (δ_1) and for dielectric (δ_2) as

$$\delta_1=\frac{1}{|\kappa_1|}=\frac{\lambda}{2\pi}\left|\cdot\frac{\varepsilon_1'+\varepsilon_2}{\varepsilon_1'^2},\right|^{1/2} \text{ and}$$

$$\delta_2=\frac{1}{|\kappa_2|}=\frac{\lambda}{2\pi}\left|\cdot\frac{\varepsilon_1'+\varepsilon_2}{\varepsilon_2^2},\right|^{1/2} \quad \text{(eq. 3.1)}$$

which comes from the relation

$$\kappa_1 = \cdot \varepsilon_1 \frac{\omega^2}{c^2} - k_x^2 ,^{1/2} \quad \text{and} \quad \kappa_2 = \cdot \varepsilon_2 \frac{\omega^2}{c^2} - k_x^2 ,^{1/2}, \quad \text{(eq. 3.2)}$$

together with plasmon dispersion Eq. (1.1). Therefore, if we take 1 as gold and 2 as water at λ=750 nm, each penetration depth of the field in both sides is

$$\varepsilon'_1 = \varepsilon'_{Au} = -20.98, \ \varepsilon''_1 = \varepsilon''_{Au} = 1.541$$
$$\varepsilon'_2 = \varepsilon'_{Water} = 1.767, \ \varepsilon''_2 = \varepsilon''_{Water} = 0$$
$$\delta_1 = \cdot \frac{1}{\kappa_1} , = 24.94 \text{ nm, and } \delta_2 = \cdot \frac{1}{\kappa_2} , = 296.15 \text{ nm.} \quad \text{(eq. 3.3)}$$

But if we take a shorter wavelength, say at λ=650 nm, they will become

$$\varepsilon'_1 = \varepsilon'_{Au} = -9.697, \ \varepsilon''_1 = \varepsilon''_{Au} = 1.044$$
$$\varepsilon'_2 = \varepsilon'_{Water} = 1.772, \ \varepsilon''_2 = \varepsilon''_{Water} = 0$$
$$\delta_1 = \cdot \frac{1}{\kappa_1} , = 30.03 \text{ nm, and } \delta_2 = \cdot \frac{1}{\kappa_2} , = 164.34 \text{ nm.} \quad \text{(eq. 3.4)}$$

From the discussions above, we can manipulate penetration depth and so the sensitivity by selecting an appropriate wavelength.

Angle- and Wavelength -Interrogated SPR Sensor System

Eq. 1.4 shows possible SPR interrogation methods; the first is to vary incident angle at a fixed wavelength when dielectric function ε_2 has changed due to the thickness or refractive index change, while the second is to vary wavelength at a fixed angle to retain plasmon-coupling condition. Each of the methods has its own benefits and deficiencies, for example, the use of goniometer for the first case, while the use of spectrometer for the second case. Other important parameters are sensor layer configuration, dynamic range of incident angle, and wavelength. Most of the refractive index in aqueous phase (e.g. buffer solution) has at least 1.33 and up, one must take into account these parameters in selecting an appropriate angle and wavelength range.

Figure 3(A) depicts SPR angle as a function of refractive index change $n_2 = \sqrt{\varepsilon_2}$ for two different wavelength (λ=632.8 nm and λ=830 nm), which were obtained from Fresnel calculations. We assumed BK7 glass as prism material, and on top of the prism 2 nm chromium layer and 50 nm gold layers were vacuum-deposited successively. Refractive index (RI) of dielectric material adjacent to gold layer is assumed to be changed from about 1.33 up to 1.40. From

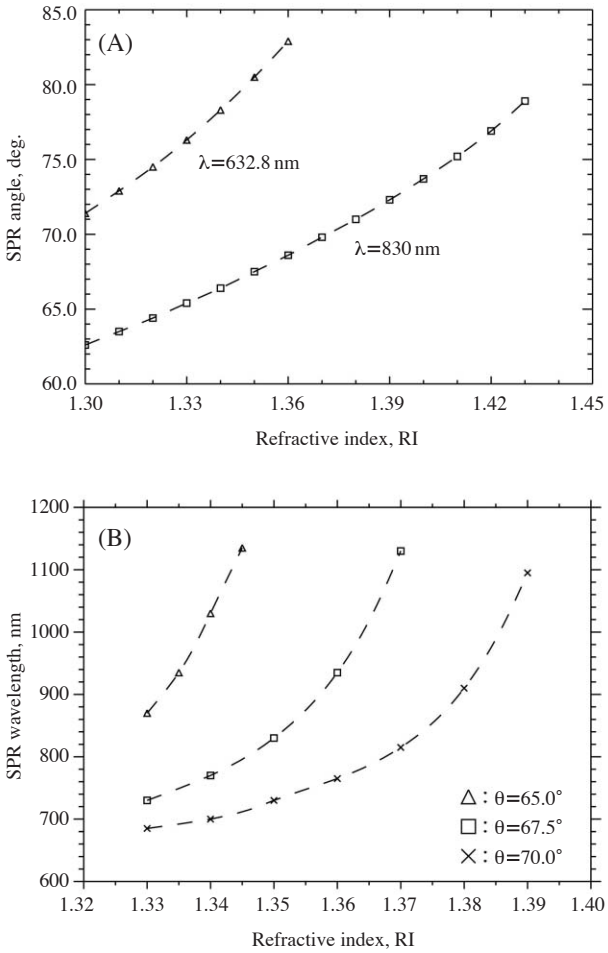

Figure 3. (A) Simulated SPR angle as a function of refractive index change for λ=632.8 nm and λ=830 nm, calculated from Fresnel equation. SPR sensor configuration is BK7/2 nm Cr/50 nm Au/X, where RI of X varies from 1.30 to 1.43. (B) Simulated SPR wavelength change as a function of refractive index for different incident angle. Also calculated from Fresnel equation.

Figure 3(A) it is clear that if we want to monitor a wide range of RI, it is beneficial to take a longer wavelength, at the cost of smaller SPR angle change. Since the pedestal of SPR angle changes drastically for the given wavelength, which is about 71.3° for 632.8 nm and 62.6° for 830 nm respectively, it is necessary to determine dynamic range of RI to be monitored *a priori*, before selection of design parameters such as incident angle and wavelength.

As the same sense, Figure 3(B) shows SPR wavelength change as a function of refractive index for different incident angle. It also shows that it is better to take a larger incident angle for a wider range of RI monitoring.

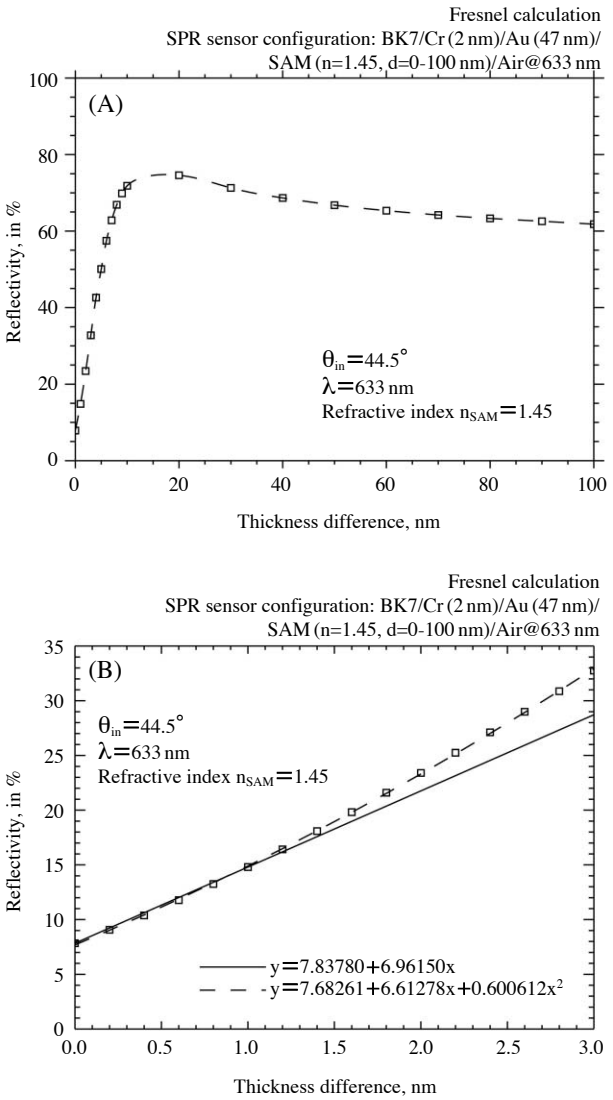

Figure 4. (A) Simulated, theoretically calculated percent-reflectivity (%ΔR) as a function of self-assembled monolayer (SAM) thickness adsorbed on gold surface. Assumed (effective) RI of SAM is 1.45 and SPR sensor configuration is BK7/Cr 2 nm/Au 47 nm/SAM 1-100 nm. (B) Magnified view of (A) showing the valid region of linearity, up to 1 nm thickness of SAM layer.

SPR Imaging

SPR Intensity Imaging

Assume that if a monochromatic light is illuminated on metal layer through a prism, not on a point, but on the whole surface at a fixed wavelength. Then, reflectivity of each point on the surface differs from each other, according to off-resonance conditions. Therefore, if a well-collimated, an expanded and an incoherent light is used, one can construct a two-dimensional SPR intensity imaging system. Such a SPR imaging system has features of great benefits over conventional angle- or wavelength-interrogated SPR sensor system, for example, to monitor RI changes simultaneously for independent, multiplexed detection zones.

However, essentially the SPR intensity imaging obtains information about RI change of adsorbed layer from a *relative* reflectivity difference at one point on the metal surface: To estimate *absolute* RI- or thickness change of a dielectric on the metal layer point by point, at least one *absolute* reflectivity data as a function of angle or wavelength, is needed.

More critical drawback of the SPR intensity imaging is signal proportionality. In using and in interpreting SPR intensity imaging, one usually takes a *linear region* of the reflectivity, at around 30% of full reflectivity signal, for example, to monitor affinity kinetics of each detection zone. In reality, however, so-called *linear region* of the reflectivity strongly depends on sensor configuration, sorts of metal and dielectric, and on layer thickness. Figure 4(A) is a simulated, theoretically calculated percent-reflectivity (% ΔR) as a function of self-assembled monolayer (SAM) thickness adsorbed on gold surface. Assumed (effective) RI of SAM is 1.45 and SPR sensor configuration is BK7/Cr 2 nm/Au 47 nm/SAM 1-100 nm. From the figure we easily see that proportional region in which relative reflectivity increases as SAM layer thickness increases is up to 15 nm. Beyond this value, the reflectivity slowly goes down.

Also the linearity of the reflectivity signal vs. thickness change of adsorbed layer is limited within ca. 1 nm, as shown in Figure 4(B). So the valid response region must be always examined for correct interpretation of sensor signal in SPR intensity imaging.

SPR Angle Imaging

One another type of SPR imaging, though retaining absolute calibration capability of thickness change and multiplexed detection, is SPR angle imaging; one can obtain SPR angle change for individual detection zone by using a wedge-shaped beam of monochromatic light, focused on a hemi-cylindrical prism. Because light is wedge-type, dynamic range of incident angle is determined by beam expansion dimension. If the SPR angle is within this angle range, reflected light projected on a two-dimensional sensor, e.g., on a CCD, build a dark band that corresponds to SPR dip line. By taking a cross-section of the image along the expanded beam and by fitting experimental data to the reflectivity as a function of angle, which was theoretically obtained from Fresnel equation, one can

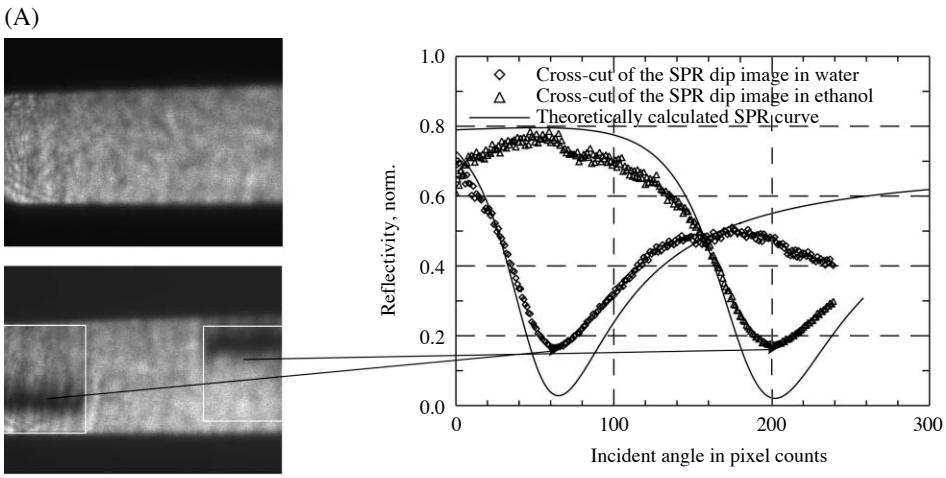

Figure 5. (A) An example of SPR angle images, obtained from a SPR angle imaging system. As a sample liquid, we took water (n_D=1.33) and ethanol (n_D=1.36) for calibration of the system. ROI is 150 × 240 pixels, as indicated in squares on the left image. Theoretical reflectivity functions tuned to the experimental values from SPR angle iages is also shown. (B) Over-plot of SPR curve obtained from cross-cut of SPR angle image, re-scaled in angle, on theoretical values.

estimate thickness change of dielectric adsorbed on metal layer.

Different from SPR intensity imaging, SPR angle imaging is capable of absolute calibration for thickness change, because we can obtain reflectivity vs. angle curve from the cross-cut of the image in *absolute* measure, though in pixel counts.

Scaling and Calibration from Pixel Counts to Angle

Once we take a region-of-interest (ROI) from the image, we can define dynamic range of SPR angle change in pixel counts. To estimate absolute thickness change it is essential to re-scale the units of pixel counts to angle. Figure 5(A) is an example of SPR angle images, obtained from a SPR angle imaging system. As a sample liquid, we took water (n_D=1.33) and ethanol (n_D=1.36) for calibration of the system and ROI is 150 × 240 pixels, as indicated in squares. Because ROI that we take from the images is essentially arbitrary, one is needed to tune the experimental reflectivity values obtained from cross-cut of image to theoretical values of reflectivity for at least two points, e.g., the minima of reflectivity. Then reflectivity curves as a function of pixel counts are obtained, and this can be re-scaled to a function of incident angle via a polynomial fit. In case of third-order polynomial

$$\theta(p)=\theta_0+c_1p+c_2p^2+c_3p^3 \qquad \text{(eq. 5.1)}$$

where p is pixel counts c_1, c_2 and c_3 are expansion coefficients, we obtain

$$\theta_0=62.52,\ c_1=1.37\times10^{-2},\ c_2=5.22\times10^{-5},\ c_3=-1.31\times10^{-7}. \qquad \text{(eq. 5.2)}$$

Figure 5(B) depicts an over-plot of SPR curve obtained from cross-cut of SPR angle image, re-scaled in angle, on theoretical values. After calibration from pixel counts to angle, SPR angle difference between ethanol and water can be calculates as

$$\Delta\theta = \theta_{SPR}(\text{ethanol}) - \theta_{SPR}(\text{water})$$
$$= \left[\cdot \frac{\Delta\theta}{\Delta p}, _{p=p_{ethanol}} \times p_{ethanol} - \cdot \frac{\Delta\theta}{\Delta p}, _{p=p_{water}} \times p_{water} \right]$$
$$= 2.61^\circ \qquad \text{(eq. 5.3)}$$

which differs from theoretically calculated value $\Delta\theta = 2.8^\circ$. First of all, discrepancy in SPR angle change might come from the quality of image. Light source that we have used in the experiments is a near-IR laser diode with $\lambda = 850$ nm, which produces speckles on the image due to long coherence length. Consequently, boundaries of SPR dip line will smear so that it is difficult to obtain a reasonable ROI range.

Localized Surface Plasmon Resonance

The term "surface" in SPR can be interpreted in different manner, according to the geometry and configuration of plasmon-supporting metal. In the preceding sections we have considered a two-dimensional, nanometer-thick metal layer which is bound longitudinally, say in z-direction, whereas not bound in spatial direction, in (x, y)-plane. Now, if we shrink geometry of metal layer down to nanometer scale in both x- and y-directions, two-dimensional metal layer becomes a zero-dimensional, a nano-sized metal particle. Free electron movement in such a very small particle is then strongly confined such that the size of metallic particles is smaller than average mean free path of the electrons. In this case, particles show a strong extinction maximum due to the plasmon resonance. This particle plasmons or localized surface plasmons (LSPs) are a polarization mode of electrons in and on the surface of metallic nanoparticles.

As a model system one usually consider a metallic nanosphere which is made of noble metal (Au, Ag, etc.), immersed in a dielectric ambient. In 1908, Gustav Mie solved this problem using Maxwell equations with symmetry conditions of wavefunctions[5]. This model was a strongly simplified model, but it still gives us profound insights into optical properties of metallic nanoparticles, independent of their shape.

An ensemble of metallic nanoparticles, mostly of gold, has a distinctive plasmon resonance character in visible region. Resonance peak in extinction and in scattering cross-section can be changed, if dielectric

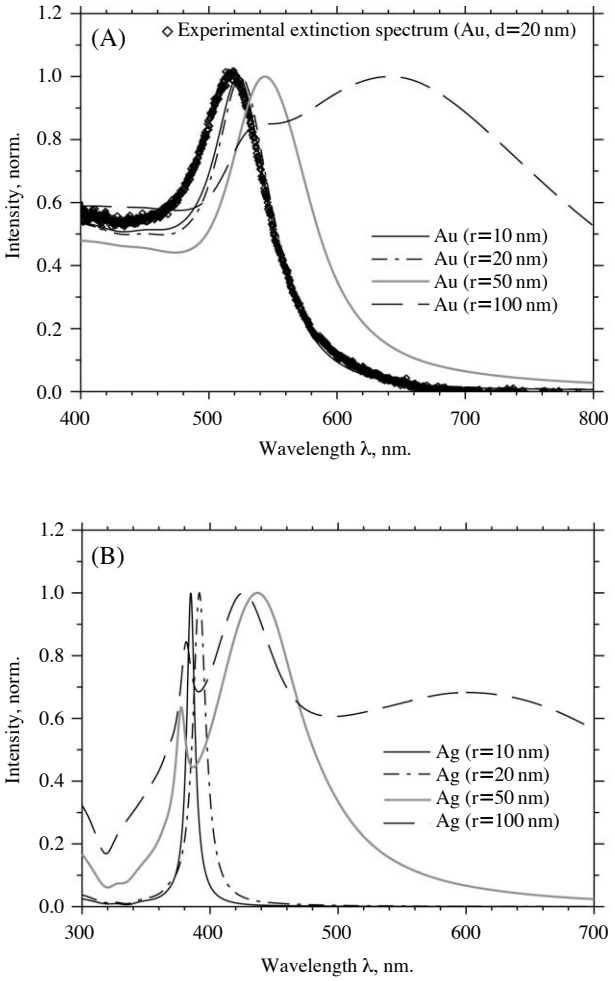

Figure 6. (A) Calculated extinction spectra in visible region for different size of gold nanoparticles, based on Mie scattering theory. Assumed are gold nanoparticles, various in size, mono-dispersed in water. Also depicted is a measured extinction spectrum for colloidal gold nanoparticles with an average size of ca. 20 nm (Sigma G1652-20M). (B) Same as (A), but for silver nanoparticles.

conditions (refractive index or thickness) of dielectric material has changed which is adsorbed on the metallic particles. For example, if biomolecules are adsorbed on the metallic nanoparticles, refractive index will change locally on metal surface. This induces changes in localized plasmon resonance condition, leading in the shift of extinction wavelength.

From Mie theory, scattering coefficients are given as the ratio of two Wronskian determinants of linear independent wavefunctions as[6,7]

$$a_n = \frac{m\psi_n(mx)\psi_n'(x) - \psi_n(x)\psi_n'(mx)}{m\psi_n(mx)\xi_n'(x) - \xi_n(x)\psi_n'(mx)}$$

$$b_n=\frac{\psi_n(mx)\psi_n'(x)-m\psi_n(x)\psi_n'(mx)}{\psi_n(mx)\xi_n'(x)-m\xi_n(x)\psi_n'(mx)}\ , \qquad \text{(eq. 6.1)}$$

where the size parameter x and the ratio of metal and dielectric refractive index m is given as

$$x=ka=\frac{2\pi a}{\lambda},\ m=\frac{N_p}{N_h}=\frac{\text{RI of the particles}}{\text{RI of the host matrix}}$$

$$\psi_n(x)=xj_n(x),\ \xi_n(x)=xh_n^{(1)}(x) \qquad \text{(eq. 6.2)}$$

and $j_n(x)$ and $h_n^{(1)}(x)$ is Ricatti-Bessel- and Ricatti-Hankel function of 1st kind, respectively. From Eqs. (6.1) and (6.2) one can calculate extinction- and scattering cross-sections using the formulae

$$Q_{SC}=\frac{2}{x^2}\sum_{n=1}^{\infty}(2n+1)\{|a_n|^2+|b_n|^2\}$$

$$Q_{EXT}=\frac{2}{x^2}\sum_{n=1}^{\infty}(2n+1)\{\mathrm{Re}(a_n+b_n)\}$$

$$Q_{ABS}=Q_{EXT}-Q_{SC}$$

$$Q_{NF}=2\sum_{n=1}^{\infty}\left\{\begin{matrix}|a_n|^2[(n+1)|h_{n-1}^{(2)}(x)|^2+n|h_{n+1}^{(2)}(x)|^2\\+(2n+1)|b_n|^2|h_n^{(2)}(x)|^2\end{matrix}\right\}_{sp} \qquad \text{(eq. 6.3)}$$

where Q_{SC}, Q_{EXT} and Q_{ABS} is scattering-, extinction-, and absorption scattering cross-section, respectively. Messinger *et al*. calculated near field extinction cross-section Q_{NF} from Mie theory[7].

Figure 6(A) shows extinction spectra Q_{EXT} in visible region for different size of gold nanoparticles, based on Mie scattering theory. Assumed are gold nanoparticles, mono-dispersed in water. For 10 nm radius gold nanoparticles extinction peak appears around 523 nm, while for 50 nm radius particles it appears at 544 nm. From this result we immediately recognize that for lager particle size, plasmon resonance wavelength shifts to the longer one. For comparison, we measured also extinction spectrum of colloidal gold nanoparticles, which have an average size of ca. 20 nm (Sigma G1652-20M). This experimental extinction cross-section was over- plotted on the same figure (diamond polymarkers). Figure 6(B) is the same extinction spectra, although for silver nanoparticles with various sizes. Plasmon resonance peak for silver particles is shifted to shorter wavelength and shape of resonance peak is more symmetric, because contribution from interband transition moves to the UV region.

Conclusion

In this paper, we revisited and examined some basic, yet critical characteristics of plasmonic biosensor. Starting from physical principles of surface plasmons, dispersion relations, and resonant coupling conditions of light to plasmon modes, we further discussed on dispersion data, of which the correctness is essential for theoretical simulation and determination of design parameters. Penetration depth of plasmon fields were calculated for representative situations. Functional as well as structural differences between difference intensity- and angle imaging of SPR system were clarified. In a SPR angle imaging system, for absolute calibration of thickness or refractive index change of dielectric on metal layer, a scaling procedure from pixel counts to angle value was demonstrated. Lastly, physical background of resonant extinction cross-section of metallic nanoparticles was briefly explained, based on Mie scattering. Distorted- and free wavefunctions are employed in scattering coefficients, which make possible to calculate extinction-, scattering-, as well as near-field cross-sections. These observables were theoretically calculated for various size of gold and silver nanoparticles, and compared with experimentally observed extinction spectra for colloidal gold nanoparticles.

Acknowledgement

This work was supported in part by the Ministry of Information and Communication Korea, under grant 07MB2710.

References

1. Raether, H. Surface Plasmons (Springer, Berlin, 1988).
2. Agranovich, V.M. & Mills, D.H. Surface Plasmons: Electromagnetic Waves at Surfaces and Interfaces (North-Holland: Amsterdam, 1982).
3. Johnson, P.B. & Christy, R.W.P. Optical constants of the noble metals. *Phys. Rev. B.* **6**(12), 4370-4379 (1972).
4. Palik, E. D. (Ed.), Handbook of Optical Constants of Solids Vol. I, II & III (Academic Press, New York, 1998).
5. Mie, G. Beiträge zur optik trüber medien, speziell kolloidaler metallösungen. *Ann Phys.* **25**, 377-445 (1908).
6. Bohren, C. & Huffman, D.F. Absorption and Scattering of Light by Small Particles (John Wiley & Sons: New York, 1983).
7. Messinger, B.J., von. Raben, K.U., Chang, R.K. & Barber. P.W. Local fields at the surface of noble-metal microspheres. *Phys. Rev. B.* **24**, 649-657 (1981).